INL/RPT-24-78326
Revision 0

Melt Crystallization of CsF from Alkali Fluorides

May 2024

Kevin R. Tolman
María Del Rocío Rodríguez-Laguna
Jacob A. Yingling
Tae-Sic Yoo

Idaho National Laboratory

INL is a U.S. Department of Energy National Laboratory
operated by Battelle Energy Alliance, LLC

Page intentionally left blank

Table of Contents

1. Introduction

Fractional melt-crystallization is a technique used to separate components in a multicomponent liquid mixture through controlled cooling. In fiscal year (FY) 2023, this technique was successfully used to separate CsCl from LiCl-KCl (Rodríguez-Laguna et al., 2024). This demonstrated a potential route for concentrating electrorefiner fission product waste streams in pyrochemical fuel cycles, building on previous work that developed the melt-crystallization system for fission product removal from LiCl-based electrolytes used for oxide reduction (Williams et al., 2013; Cho et al., 2010; Versey et al. 2014).

In this FY 2023 study, thermodynamic calculations indicated that a thermally controlled solid-liquid separation method could recover up to 92.8% of the initial cesium chloride. Experimental recovery of CsCl from a chloride salt matrix (CsCl-NaCl-LiCl-KCl) was demonstrated using a two-heat-source crystallizer. Elemental analysis of the liquid fraction showed that cesium concentrated in the liquid portion of the solid-liquid separation. Additionally, X-ray diffraction (XRD) data taken at room and high temperatures revealed that the initial solid fraction did not contain any crystalline phase with cesium.

Another notable application of molten halides is in molten salt reactors (MSRs), which often utilize fluoride-based molten salt systems. In these reactors, the group I and II fission products (Rb, Cs, Sr and Ba), as well as the lanthanide fission products, I, Se, and Te accumulate in the fuel salt. Developing a successful fuel cycle for fluoride-based MSRs will require the implementation of various separation technologies targeted at the specific chemical properties of these fission products.

To assess the feasibility of extending fractional melt-crystallization technology to MSR applications, similar experiments were performed in fluoride melts for FY24. This is an important step towards leveraging existing pyrochemical fuel cycle technologies to develop fuel cycles applicable to MSRs.

Specifically, this work investigated whether a thermally controlled process of a solid-liquid separation process could effectively remove CsF from LiF-NaF-KF (FLiNaK)-CsF salt for MSR fuel cycle applications. The designed process aimed to recover purified LiF-NaF-KF salt as solid precipitates while

concentrating CsF to a remaining salt heel. This concentrated CsF can then be immobilized during a salt waste stream treatment operation, minimizing waste volume.

Following the procedure established in chloride system studies, thermodynamic calculations were conducted to theoretically assess the separation feasibility. Upon confirmation, a two-heat-source melt-crystallizer was utilized to collect liquid samples at various stages of the partial-crystallization process. The liquid phase behavior was examined using inductively coupled plasma mass spectroscopy (ICP-MS) analysis. Additionally, the phase behavior of the FLiNaK-CsF system was investigated using differential scanning calorimetry (DSC) and high-temperature X-ray diffraction (HT-XRD).

2. Methodology

Chemicals

Cesium fluoride (>99.9%, Sigma Aldrich), sodium fluoride (>99.995%, BTC), lithium fluoride (>99.95%, BTC), and potassium fluoride (99.9%, Thermo Scientific) were used. Throughout the investigation, the chemicals were handled inside an inert argon-atmosphere glovebox.

Composition

A quaternary LiF-NaF-KF-CsF mixture was prepared using 10 wt. % CsF. The individual salts were dried using a slow heating rate, allowing moisture to be removed gradually from room temperature up to 350 °C for more than 80 hr, through a series of controlled isothermal steps. FLiNaK eutectic (46.5 LiF, 42 KF, 11.5 NaF, mol %) was prepared by blending the mixture in a glassy carbon crucible, then placed inside a muffle furnace within an argon-atmosphere glovebox. The temperature was increased at a rate of 10 °C· min^{-1} up to 900 °C, where it was held for 6.5 hr at atmospheric pressure. The furnace was turned off, and the sample was left inside to cool down with the furnace before being crushed with an impact mortar and pestle and finely ground with an agate mortar and pestle. Then, CsF was mixed with the FLiNaK mixture (10 CsF-90 FLiNaK, wt. %) in a glassy carbon crucible, and heated up to 700 °C at a heating rate of 10 °C· min^{-1} inside a muffle furnace within an argon-atmosphere glovebox, where it was held at this temperature for 2hr. The furnace was turned off, and the sample was left inside to cool down with the furnace before being crushed with an impact mortar. The sample composition is as follows 26.3 % LiF, 53.2 % KF, 10.5 % NaF, and 10 % CsF by weight, where the FLiNaK eutectic proportion was maintained.

The sample mass before and after the thermal treatment remained unchanged. There was no indication of salt vaporizing from the molten salt in the crucible during heating, suggesting that the initial moisture content was likely minimal. The salt was melted and crushed prior to sampling for analysis.

Characterization techniques

Elemental analysis was conducted using inductively coupled plasma mass spectrometry (ICP-MS) with an Agilent 7900 instrument. Each sample's mass was recorded, followed by the addition of 25 mL of 8% HNO_3 acid solution (trace-metal grade, Fisher Scientific). After complete dissolution, samples were brought up to a 50 mL volume using ultra-pure water (18.2 MΩ cm^{-1}, Millipore). Subsequently, a series of dilutions were prepared from the 50 mL solutions, with analysis results obtained from dilutions of 1:1,000 and 1:10,000. The Li and Cs were analyzed with a calibration from 0 to 60 ppb in 2% HNO_3 and the spike added was 10 ppb for each element. The Na and K were analyzed with a calibration from 0 to 1000 ppb in 2% HNO_3 and the spike added was 100 ppb for each element. Both analyses were done with

the addition of He gas in the “collision” mode.

Powder X-ray diffraction (XRD) data were acquired using Bragg-Brentano geometry monochromatic Cu-Kα beam radiation diffractometers (λ = 1.540593 Å). The Aeris diffractometer was equipped with an X-ray tube source and optics similar to the Empyrean diffractometer; however, the Aeris goniometer was smaller and more compact (i.e., a radius of 145 mm) than the Empyrean goniometer. The Aeris parameters included voltage and current values of 40-kV and 15-mA, respectively, PIXcel1D line detector with a Ni Kβ filter of 0.02 mm, Soller slits of 0.04 rad, and sample-holder spinner at a rotational speed of 15 rpm. XRD patterns were collected from 5 to 80 degrees 2θ with a 0.0263-degree step-size interval and 200 s per step. Salt samples were hygroscopic and maintained in an inert atmosphere during XRD analysis. The samples were loaded into an Anton Paar airtight dome sample holder to keep the argon gas atmosphere around the sample. Calculations and refinements to the data were performed using HighScore Plus (Malvern-Panalytical) and the International Centre for Diffraction Database (ICDD) PDF-4+. The Empyrean diffractometer was equipped with a high-temperature stage (Anton-Paar HTK 1200N chamber), TCU 1000 N controller and Pixel 3D detector with 0.02 mm Ni filter, soller slits of 0.04 rad, anti-scatter slit of 1/40, and divergence slit of 1.125 degrees. The alumina sample holder was 0.8 mm deep with a 16 mm radius. Scans were acquired using Cu-Kα radiation, 45-kV, and 40-mA, and 2θ ranged from 5 to 80 degrees in Bragg-Brentano geometry, with step size of 0.0263 degree and 697 s per step. Scans were conducted at constant temperatures with a temperature stabilization step of 10 min before each scan to assure thermal equilibrium. The heating rate between the scans was 10 °C·min^{-1}, and the cooling rate was 50 °C·min-1. Chamber pressure was approximately $1 \cdot 10^{-1}$ bar.

Differential scanning calorimetry (DSC) was employed to investigate the thermal behavior of the systems. Calorimetric measurements were conducted using a Netzsch Simultaneous Thermal Analyzer (STA), model 449F3-0171-M heat-flux type calorimeter equipped with a type-K thermocouple which was used to obtain the DSC and thermogravimetric analysis (TGA) simultaneously. The equipment was located inside an argon glovebox with oxygen and moisture levels <10ppm and was temperature and enthalpy calibrated between 200–600 °C using Netzsch traceable standards — indium, bismuth, zinc, cesium chloride and aluminum. The DSC conditions involved employing ultra-high-purity argon for both the purging and protective gases with a gas flow of 50 ml/min. Glassy carbon crucibles of 50 µl with pierced lids were used for the reference, standards, and salt samples due to their inertness with the Li-Na-K-Cs fluoride salt.

Experimental procedures

The laboratory-scale crystallizer was placed inside an argon atmosphere glovebox. The setup consisted of a nickel crucible containing the salt, heated simultaneously by two sources: a Cole-Parmer StableTemp ceramic hot plate and a Firerod cartridge heater (Model 1044–07. 120 V, 400 W-F14, incoloy sheath) with embedded Type-K thermocouple, as shown in Figure 1. The cartridge heater’s role was to help raise and control the temperature in the center of the crucible to achieve the thermal gradients that were needed in the system. The Ni crucible was covered with a custom-made lid fabricated from a tall ceramic crucible open at the bottom, facilitating placement of the cartridge heater and thermocouple. This lid played a crucial role in reducing heat loss (Figure 1).

Figure 1. Top view of the laboratory-scale crystallizer system.

The experimental procedure involved the following steps:

1. The sample was fully melted by applying the maximum power of both a hot plate (540 °C) and cartridge heater (700 °C). These temperatures remained constant for at least 30 min.
2. The cartridge heater remained at its maximum temperature (700 °C) throughout the experiment. The hot plate was controlled to the desired temperature for sample collection.
3. Using a spatula, the liquid portion of the sample near the thermocouple was collected at various temperatures.
4. After any temperature adjustment, there was a waiting period of 10–15 min at the target temperature to ensure temperature stability.

Thermochemical calculations

The phase equilibria, transitions, and compositions of the experimental chloride salt mixtures were calculated by Gibbs energy minimization using FactSage 8.2 software. The Gibbs energy functions available in the FTSalt pure compound, FTsalt-SALTE (liquid), and FTsalt-B1 (solid) solution databases were used. The liquid and solid solution database values were calculated assuming potential two and three phase immiscibility, respectively. Gibbs energy values for the gas species were excluded since the temperatures involved result in very low equilibrium activity in the gas phase.

The FTSalt liquid solution database uses the modified quasichemical model in quadruplet approximation (MQMQA), which is advantageous for its two sublattice approach that describes the cation and anion occupancies in the melt by associating a Gibbs energy change with the creation of cation-anion first nearest-neighbor and cation-cation second nearest-neighbor structure. In this way, the MQMQA permits a semi-mechanistic description of the short-range ordering of the liquid solution, which enables the thermodynamic properties of experimentally well-known two and three component systems to be more accurately extended to calculations of higher-order unmeasured systems. For the calculations in Section 3, every solid and liquid endmember available in the Li-Na-K-Cs fluoride solution database was included in the calculations.

3. Results and discussion

3.1. Thermodynamic calculations

Figure 1 shows the phase diagram of LiF-NaF-KF-CsF with fixed KF and LiF concentrations generated with FactSage software. The weight fractions of KF and LiF were fixed at 0.53 and 0.26, respectively. The phase diagram shows the transition temperatures for the composition under study, including the solidus and liquidus temperatures for the composition of interest (i.e., 26.3 LiF, 53.2 KF, 10.5 NaF, 10.0 CsF, wt. %) designated with a vertical dashed blue line. The solidus marks the upper limit of solid formation, where the melting initiates. The liquidus indicates the lowest temperature at which the material is completely molten. The solidus and liquidus temperatures for the system are calculated to be 372.3 and 470.5 °C, respectively.

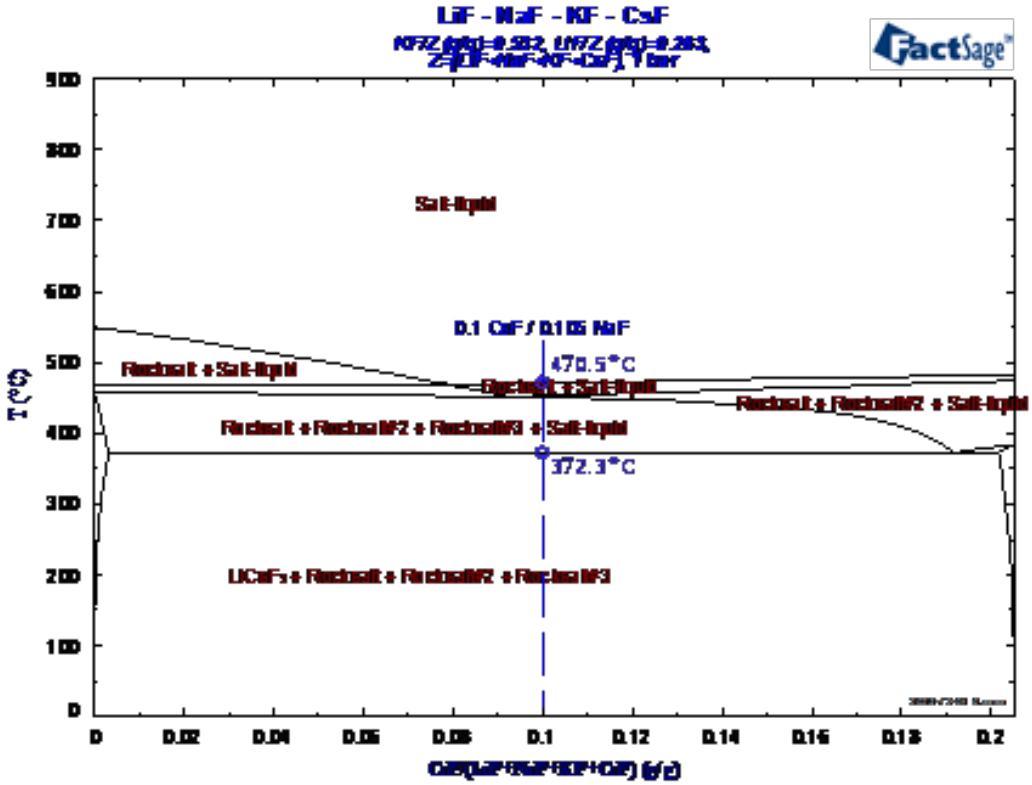

Figure 2. Phase diagram of the quaternary 53.2 KF, 26.3 LiF, NaF, CsF (wt. %) calculated with FactSage. The composition of interest is designated with a dashed blue line (composition: 53.2 KF, 26.3 LiF, 10.5NaF, 10 CsF, wt. *%).*

Thermodynamic equilibrium calculations for this salt system were calculated in 5 °C increments between 350–500 °C. Figure 3 shows the weight distribution of phases for the system composition as functions of temperature. Figure 4 (left) shows the temperature-dependent distribution of species in the liquid phase and Figure 4 (right) shows the temperature-dependent weight distribution of species in the solid phase. As the temperature decreases, Cs concentrates in the liquid phase and reaches a maximum concentration just above the solidus temperature (372.3 °C). As is evident in Figure 3, nearly the entire quantity of Cs is present as $LiCsF_2$ up to its melting temperature. Thus, right above this temperature, CsF exhibits the maximum concentration in the liquid since all other species are contained in one or more solid solutions.

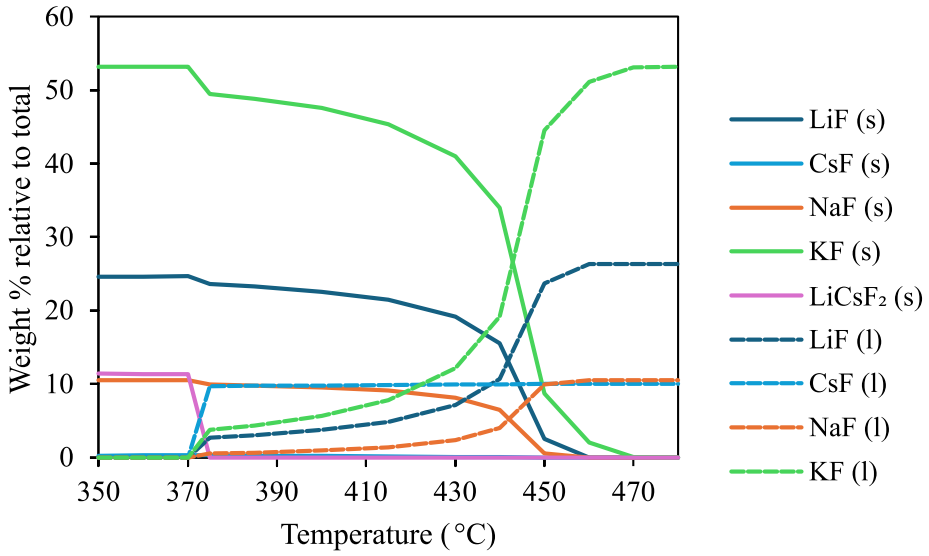

Figure 3. The distribution of species between the solid and liquid phases as a function of temperature. The weight percent of each component is relative to total sample weight. Data calculated using the FactSage equilibrium module.

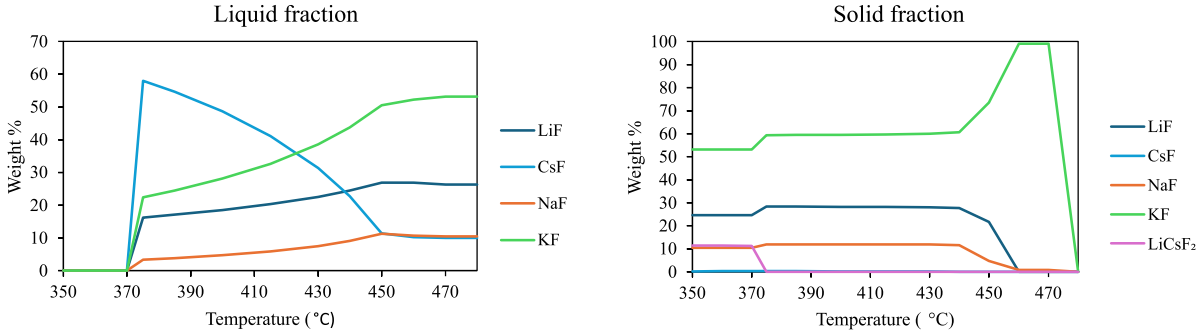

Figure 4. (left) Liquid-phase composition (liquid fraction) and (right) solid-phase composition (solid fraction) plotted as a function of temperature, calculated using the FactSage equilibrium module.

Figure 5 shows the sample liquid mass percentage with temperature — clearly indicating the solidus near 375 °C and the majority of the liquid forming as the temperature increases to the FLiNaK eutectic temperature near 455 °C. The calculations shown in Figure 2–Figure *5* indicate that there is a temperature range between 380–430 °C where a trade-off can be achieved between the removable CsF quantity and the concentration of CsF.

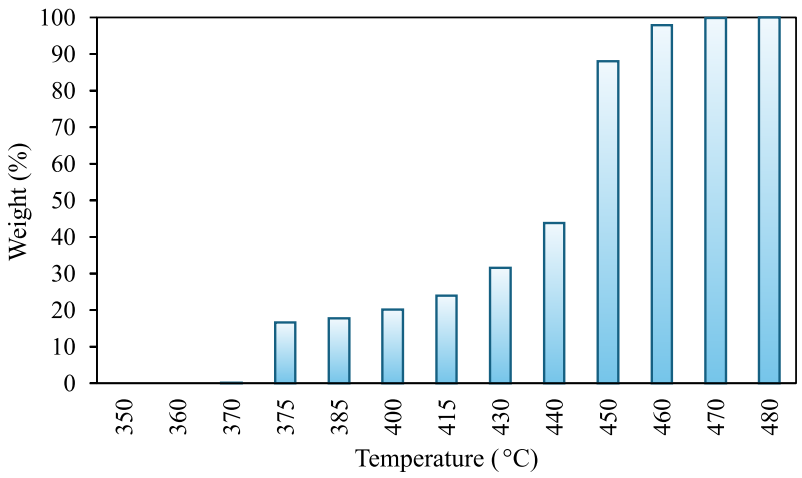

Figure 5. Liquid percentage relative to total sample weight as a function of temperature.

3.2. Experimental

Differential scanning calorimetry

Differential scanning calorimetry (DSC) was used to analyze the thermal behavior of this 90FLiNaK-10wt. %CsF system using heating curves obtained using 1, 4, 7 and 10 °C min^{-1} scan rates. In the DSC measurements, the sample's temperature changes over time according to a specific heating rate, following a predefined temperature program. In practice, thermal equilibrium conditions with DSC operations are only approximated due to several factors. Notably, there is a thermal gradient within the stagnant sample. Additionally, since temperature measurements are not taken directly from the sample, there is a thermal lag between the indicated and actual sample temperatures. This thermal lag is exacerbated at higher scan rates.

To obtain DSC measurements that approach the hypothetical thermal equilibrium, we used the DSC methodology proposed by Pedersen et al. (Pedersen et al. 2001), which involves drawing tangent lines on the baseline and peak side, at the low and high-temperature sides of the peak. This identifies the onset and endpoint temperatures, respectively (Ferreira et al. 2010). The onset and endpoint data for each scan rate are plotted and linearly extrapolated to null heating rate. This allows for the identification of the approximate equilibrium transition temperatures, which are the solidus and liquidus, respectively.

Figure 6 shows the DSC heating curves conducted at 1, 4, 7 and 10 °C min^{-1} scan rates. All four curves exhibit two complex endothermic peaks. The first one corresponds to the melting of an initial fraction of the sample and is composed of two overlapping peaks, the second corresponds to the melting of the rest of the sample. The second endothermic peak is a continuation of the first peak because the first does not go back to the baseline. This result aligns with the calculations, as the phase diagram suggests the presence of a broad "solid + liquid" region, indicating the coexistence of both solid and liquid phases over a wide temperature range. The presence of overlapping peaks suggests the occurrence of multiple phase transitions, indicating a complex phase behavior beyond two transitions. This is consistent with the calculated data shown in the phase diagrams in Figure 2.

Table 1 illustrates the DSC data, including onset and endpoint values for this system at heating rates of 1, 4, 7, and 10 °C min^{-1}. Additionally, it provides extrapolated values at zero heating rate, serving as

estimations for the solidus and liquidus temperatures. The extrapolated value for the onset at 378.6 °C (estimated solidus) is close to the calculated value at 372.3 °C (FactSage), showing a difference of approx. 6 °C. To enhance clarity and facilitate comparison, Figure 6 includes dashed lines to illustrate modeled phase-transition temperatures, while solid lines represent experimental DSC data extrapolated to zero heating rate. On the other hand, comparing the experimental liquidus (extrapolated value) of 452.9 °C with the calculated liquidus (FactSage) of 470.5 °C reveals an approximate difference of 17 °C. The curve at 1 °C min^{-1} (blue curve) in Figure 6 clearly shows a straight baseline even below 465 °C, but the liquidus is unlikely to be detected by DSC since the fraction of liquid evolved at the liquidus temperature is low.

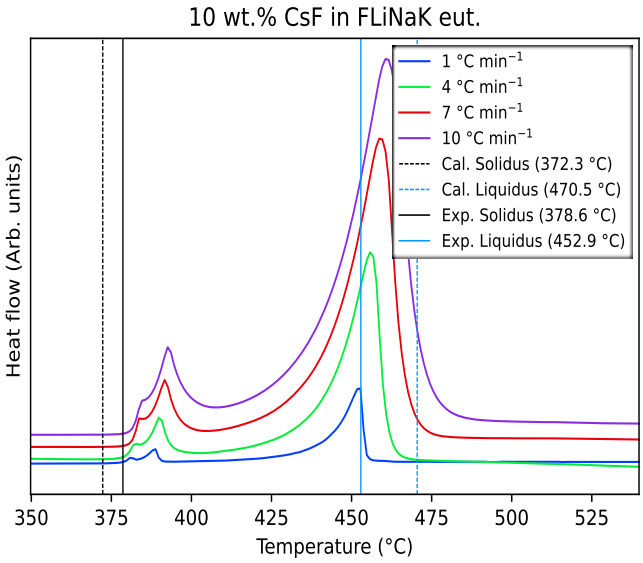

Figure 6. DSC curves corresponding to the system, conducted at a heating rate of 1 (blue), 4 (green), 7 (red), and 10 (purple) °C min^{-1}. Dashed lines indicate the modeled phase-transition temperatures. Solid lines indicate the experimental DSC data after extrapolating to 0 °C min^{-1}.

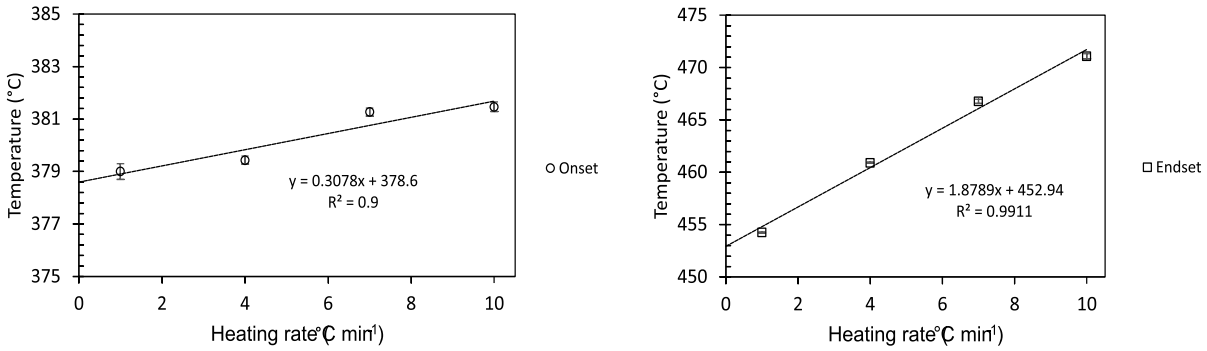

Figure 7. Average onset (*left*) and endset (*right*) values of the melting peak of the system as a function of heating rate. The error bars on measured values denote standard uncertainties, calculated from a single sample measured three times. Notably, the error bar corresponding to the value at 10 °C min^{-1} reflects the standard deviation derived from two distinct samples, each measured three times.

Table 1. DSC onset- and endset-peak data for the system (average values with standard deviation, 1σ, from a single sample measured three times, except for the value at 10 °C·min^{-1} that reflects the standard deviation derived from two distinct samples, each measured three times) at 1, 4, 7 and 10 °C·min^{-1}.

Heating rate (°C min^{-1})	Onset temperature (°C)	Endset temperature (°C)
0*	378.6	452.9
1	379.0 ± 0.3	454.3 ± 0.06
4	379.4 ± 0.15	460.9 ± 0.06
7	381.3 ± 0.15	466.8 ± 0.2
10	381.5 ± 0.18	471.1 ± 0.24

*Values extrapolated to 0 °C min^{-1}

3.2.1. Room temperature to high-temperature X-ray diffraction

The salt powder samples LiF-NaF-KF and LiF-NaF-KF-CsF were prepared for room temperature XRD. The XRD analysis of LiF-NaF-KF shown in Figure 8 reveals a multiphase salt mixture with three different phases at room temperature (RT). These three phases included a face-centered cubic (Fm-3m) lithium fluoride phase (ICDD 01-072-1538, Ott, H., Z. Kristallogr., 63, 222, 1926), a face-centered cubic (Fm-3m) sodium fluoride phase (ICDD 04-007-3591, Davey W.P., Phys. Rev., 21, 143, 1923), and a face-centered cubic (Fm-3m) potassium fluoride phase (ICDD 04-006-5358, Roche M., Montmory R., C. R. Hebd. Seances Acad. Sci., 253, 2381, 1961). Whereas the room temperature XRD pattern results for LiF-NaF-KF-CsF (Figure 9) showed a monoclinic (C2/c) cesium lithium fluoride phase (ICDD 00-022-1076, Natl. Bur. Stand. U.S. Monogr. 25, 7, 105, 1969), a face-centered cubic (Fm-3m) lithium fluoride phase (ICDD 01-072-1538, Ott, H., Z. Kristallogr., 63, 222, 1926), a face-centered cubic (Fm-3m) potassium fluoride phase (ICDD 04-006-5358, Roche M., Montmory R., C. R. Hebd. Seances Acad. Sci., 253, 2381, 1961), and a face-centered cubic (Fm-3m) sodium fluoride phase (ICDD 04-007-3591, Davey W.P., Phys. Rev., 21, 143, 1923). Thermodynamic calculations at room temperature predict the presence of three rock salt (cubic) phases and a monoclinic $LiCsF_2$ phase.

Figure 10 shows the high-temperature XRD data for the system with 10 wt. % CsF. It suggests that LiF and CsF form the monoclinic phase *C2/c* $LiCsF_2$. As the temperature rises above 385 °C, the monoclinic phase is no longer apparent in the diffraction pattern, indicating a loss of crystalline structure (i.e., it becomes amorphous). At 470 °C, the entire sample becomes liquid (no crystalline structure).

Thermodynamic calculations show that above 372.3 °C (the calculated solidus temperature), the $CsLiF_2$ phase is not present (Figure 3). The HT-XRD results confirm that above 385 °C, there are no peaks for $CsLiF_2$ phase, suggesting its transition to the liquid phase. The temperature difference between the furnace thermocouple and the sample temperature in HT-XRD equipment is approximately ΔT = 5-10 °C. A decrease in $CsLiF_2$ peak intensities was observed when comparing the diffraction patterns from 375 °C to 385 °C (Figure 11), indicating a reduction in crystallinity and a transition to an amorphous phase.

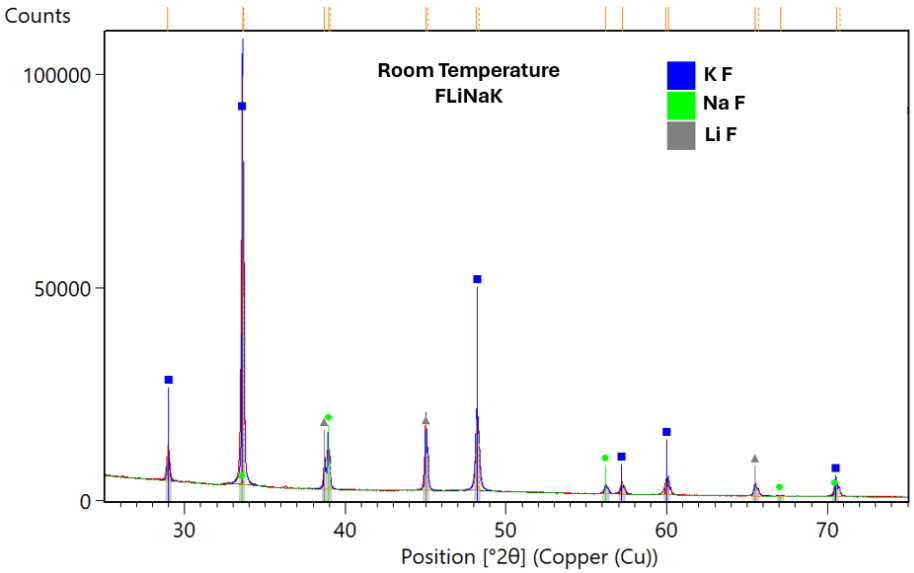

Figure 8. Room temperature diffraction pattern of FLiNaK.

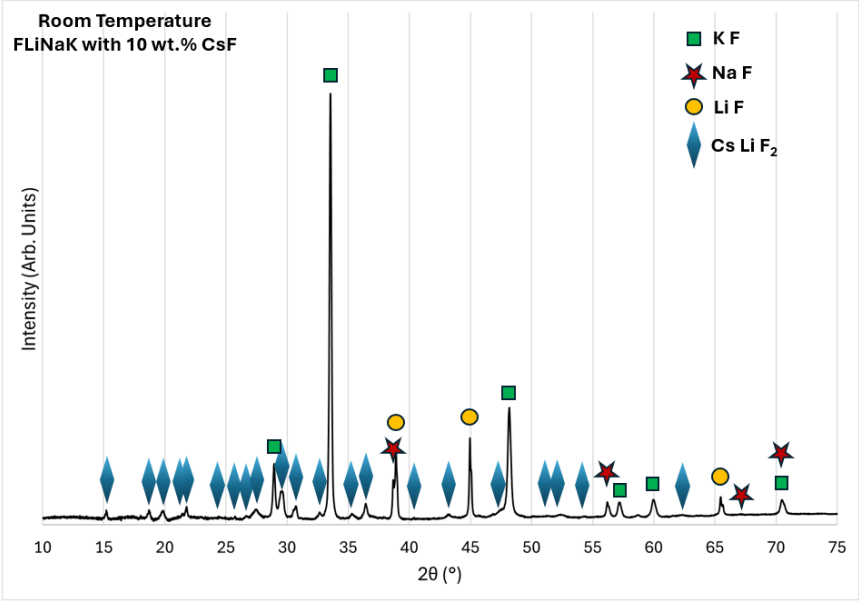

Figure 9. Room temperature diffraction pattern of FLiNaK with 10 wt. % CsF.

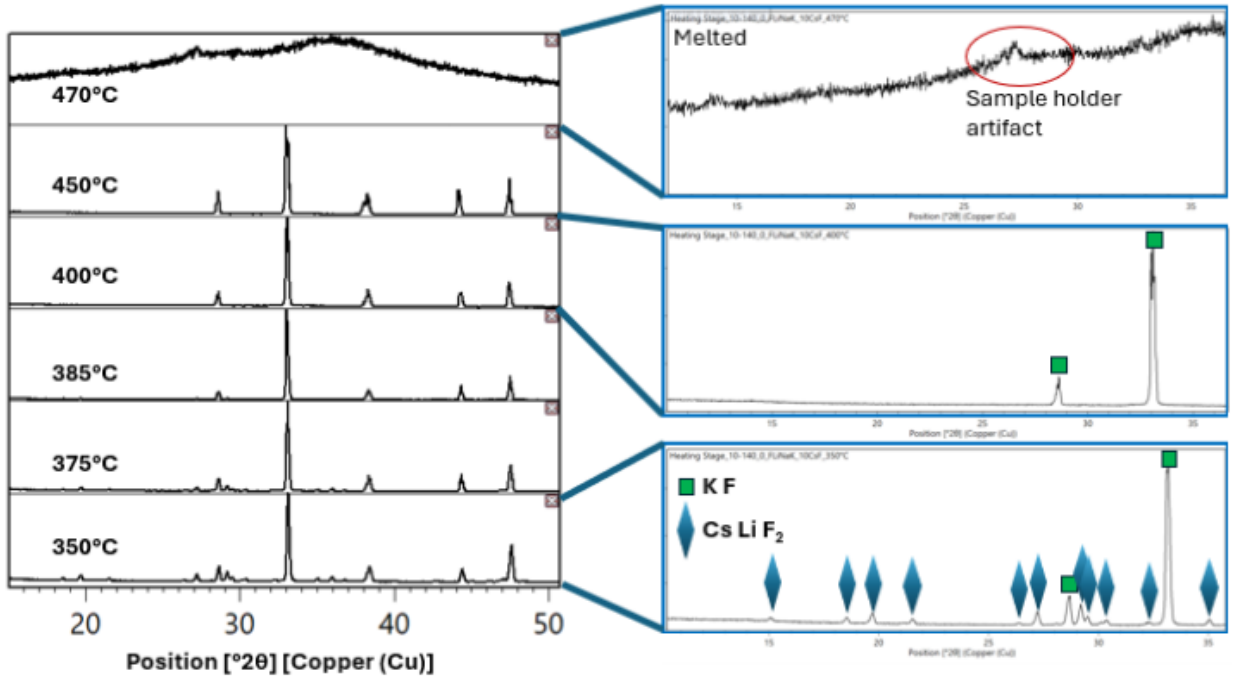

Figure 10. High temperature XRD for 90FLiNaK-10CsF shows that the sample is completely melted before 470 °C.

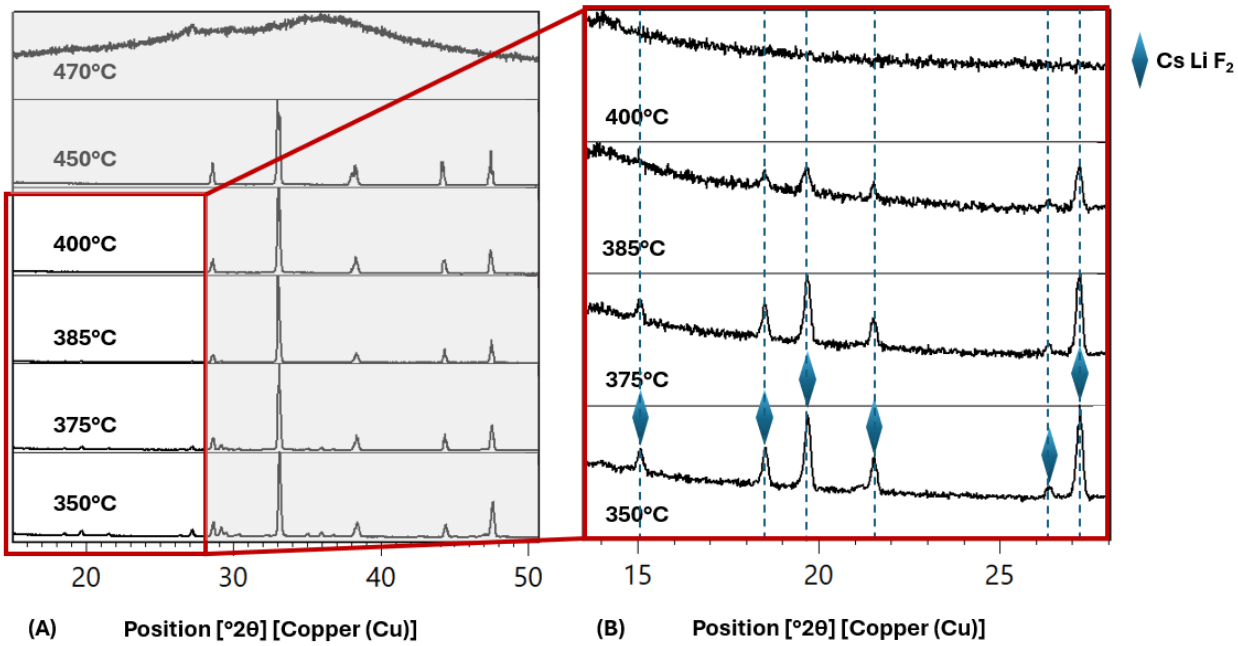

Figure 11. High temperature XRD showing that the $CsLiF_2$ phase has melted at or above 385 °C.

3.2.2. Laboratory-scale crystallizer experiment [hot finger] and elemental analysis

The laboratory-scale melt-crystallizer system offers clear visibility of both the solid and liquid fractions, facilitating the collection of liquid samples. The liquid portion of the sample was collected at different

temperatures upon crucible cooling. Figure 12 shows the ICP-MS elemental-analysis results corresponding with the collected liquid portions. The weight percent of the collected portion was plotted against the thermocouple temperature, which was close to the location where the sample was retrieved. The results revealed that at lower temperatures, characterized by a higher solid fraction in the crucible, the liquid portion exhibits a higher Cs concentration compared to samples collected at higher temperatures, where the liquid fraction predominates. In Figure 12, the left plot shows the weight percent of the collected liquid portion versus the thermocouple temperature, providing a zoomed-in version. Zoomed-in version does not show potassium values.

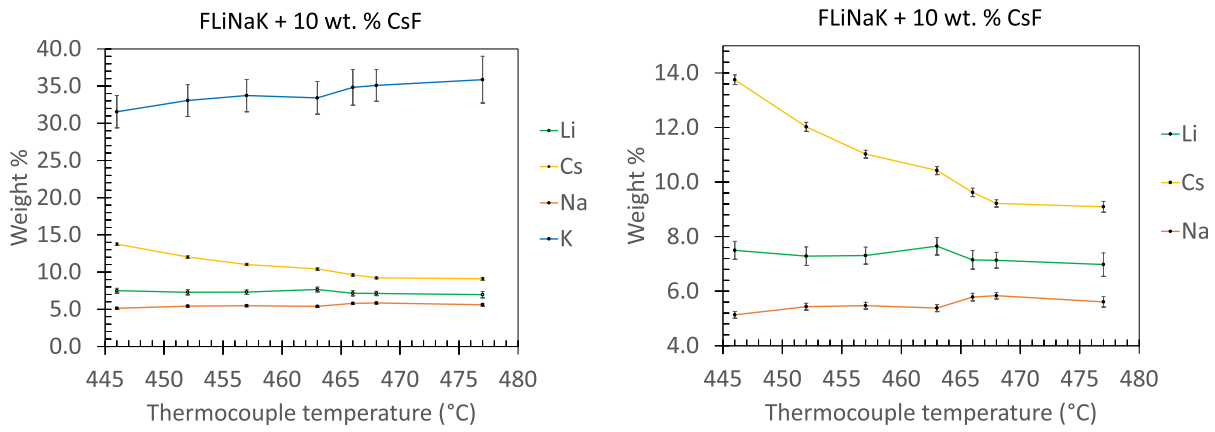

Figure 12. *Left:* Atomic-weight percent of the collected liquid portion versus the thermocouple temperature*, showcasing n*ormalized data with uncertainty. *Right: Zoomed-in view of the left figure.*

FactSage's equilibrium module was used to perform thermodynamic equilibrium calculations and predicted the composition and phase stabilities at selected conditions (i.e., to calculate the composition of the liquid and solid fractions as a function of temperature). Figure 13 shows the concentration in weight percent of the liquid portion as a function of temperature, calculated using FactSage thermodynamic software. It is observed that the concentration of Cs in the liquid fraction is higher at lower temperatures compared to higher temperatures. Both the modeled and experimental data exhibit this trend. The calculations also showed that from room temperature up to the solidus temperature, Cs was in the form of $CsLiF_2$. Above the solidus temperature the $CsLiF_2$ phase was not present, indicating a high affinity of Cs for the liquid phase. As the temperature decreased, CsCl concentrated in the liquid phase, while concentrations of the other species decreased. Based on these calculation results, the primary goal of the experimental process using the laboratory-scale crystallizer was to maximize the concentration of CsCl in the liquid phase. Figure 14 shows the atomic-weight percentage values for each element in the original composition (theoretical) compared to the experimental values obtained from elemental analysis of the system when fully molten. The plot shows that both the theoretical and experimental composition are very similar. These results confirm that the sample was completely molten, and that the actual composition of the system closely matches the theoretical composition. Therefore, any uncertainties arising from impurities in the salts, mixture preparation, or elemental analysis can be considered negligible.

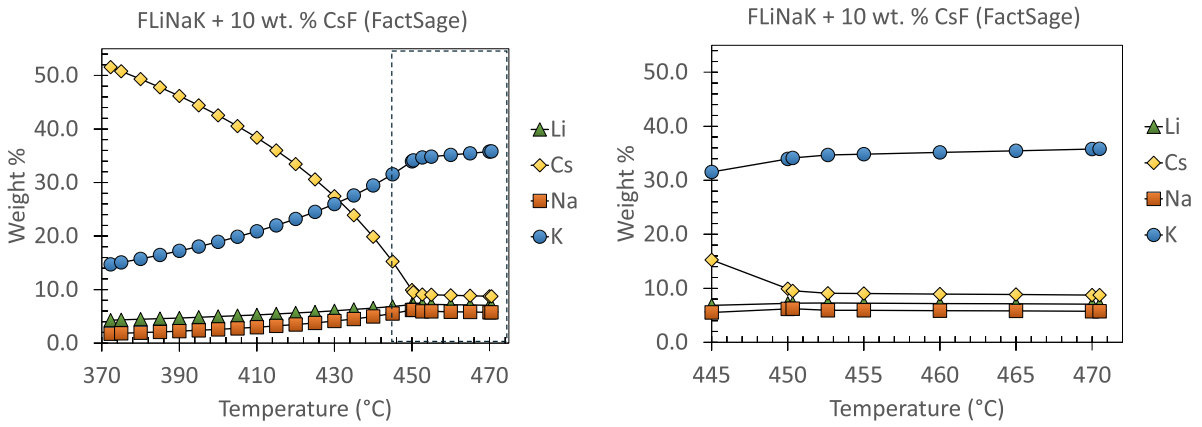

Figure 13. Left: Atomic-weight percent of the liquid portion as a function of temperature, calculated using FactSage thermodynamic software. The black rectangle indicates the temperature range measured by the thermocouple in the cartridge-heater experiment (see Figure 12 to compare trend). F was not included in the plot, which would account for the remaining weight %. Right: Zoomed-in view of the left figure.

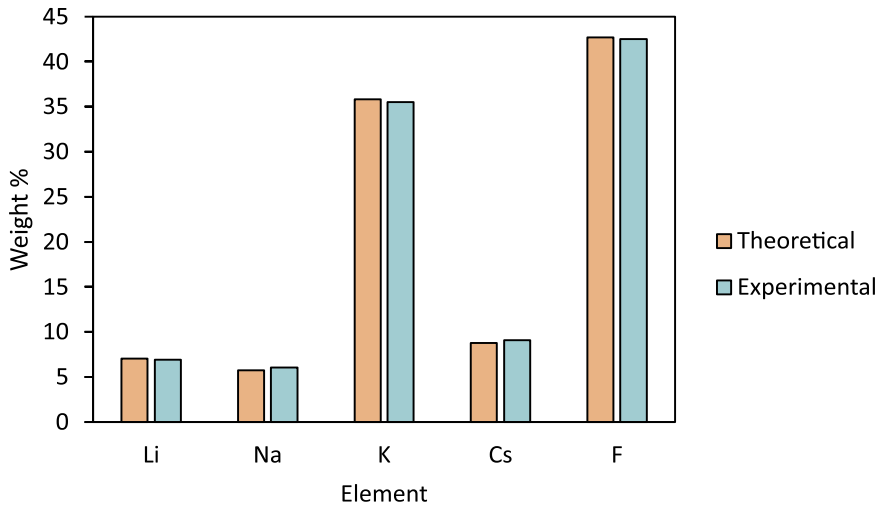

Figure 14. Atomic-weight percentage values for each element in the original composition (theoretical, brown) are compared to the experimental (blue) values obtained through elemental analysis of the liquid sample when fully molten.

4. Summary

Thermodynamic calculations showed a range of operating temperatures for the effective separation of cesium from FLiNaK. These results suggest that a thermally controlled solid-liquid separation holds the potential to concentrate Cs to the liquid phase. Experimental tests were conducted to validate the efficacy of these thermodynamic calculations. These tests included DSC, XRD, and ICP-MS. DSC was employed to identify the phase transitions of the material and provide estimates of the solidus and liquidus temperatures. The experimental solidus and liquidus temperatures were compared to the calculated values, demonstrating good agreement. RT-HT-XRD data showed that at temperatures above 385 °C the diffractogram did not exhibit $CsLiF_2$ peaks, which indicated that any cesium containing phase had already melted into the liquid portion. These results indicated that upon initiation of the liquid formation, there is a total transfer of Cs^+ to the liquid phase. ICP elemental analysis indicated that Cs^+ concentrates in the liquid portion, which agrees with RT-HT-XRD data. The results shown in this report suggest that it is feasible to accumulate cesium in a liquid phase that can be separated from the solid portion up to its operational maximum concentration.

5. Future work

Certain isotopes are of interest due to their impact on neutronics and waste management. The focus on examining Cs was driven by its waste implications along with separation difficulty, but many other isotopes are also relevant in this context. These include:

- Sr-90: A strong mid-term beta emitter and highly stable divalent halide. This isotope represents a straightforward application of the previously established melt-crystallization procedure, making it a low-hanging fruit for our studies.
- Sm-149: A neutron poison and highly stable halide. While it is expected to behave similarly to Sr-90, limited data are available. The presence of multiple oxidation states (trivalent and divalent) adds further uncertainty to its behavior. Therefore, fundamental studies are required to reach the same level of understanding as for Cs.

- I-129: A long-term repository issue due to its long half-life. Its behavior and separation processes need thorough investigation due to its significant impact on long-term waste management.
- Actinides: Concentrating actinides for recycling is critical for enhancing resource utilization in nuclear fuel cycles.
- Lanthanides: These elements are abundant in fission products and pose challenges for separation and waste minimization. Understanding their behavior in various separation processes is essential.

Depending on the near-term interests of the DOE campaign, specific elements for investigation will be determined for FY-25 research efforts.

6. References

[Williams et al. 2013] Williams, Ammon N., Supathorn Phongikaroon, and Michael F. Simpson. "Separation of CsCl from a ternary CsCl–LiCl–KCl salt via a melt crystallization technique for pyroprocessing waste minimization." Chemical engineering science 89 (2013): 258-263.

[Cho et al. 2010] Cho, Yung-Zun, et al. "Concentration of cesium and strontium elements involved in a LiCl waste salt by a melt crystallization process." Nuclear Technology 171.3 (2010): 325-334.

[Rodríguez-Laguna et al. 2024] Rodríguez-Laguna, María del Rocío, et al. "Separation of fission products from high-level waste salt systems by partial crystallization: CsCl-NaCl-LiCl-KCl study." Separation and Purification Technology 332 (2024): 125602.

[Williams et al. 2013] Williams, Ammon N., Supathorn Phongikaroon, and Michael F. Simpson. "Separation of CsCl from a ternary CsCl–LiCl–KCl salt via a melt crystallization technique for pyroprocessing waste minimization." Chemical engineering science 89 (2013): 258-263.

[Shim et al. 2017] Shim, Moonsoo, et al. "Separation of Cs and Sr from LiCl-KCl eutectic salt via a zone-refining process for pyroprocessing waste salt minimization." Journal of Nuclear Materials 491 (2017): 9-17.

[Versey et al. 2014] Versey, Joshua R., Supathorn Phongikaroon, and Michael F. Simpson. "Separation of CsCl from LiCl-CsCl molten salt by cold finger melt crystallization." Nuclear engineering and Technology 46.3 (2014): 395-406.

[Pedersen et al. 2001] Pedersen, A., et al. "The determination of dynamic and equilibrium solid/liquid transformation data for Sn–Pb using DSC." Journal of thermal analysis and calorimetry 64.3 (2001): 887-894.

[Ferreira et al. 2010] Ferreira, Eduardo Bellini, Moysés L. Lima, and Edgar D. Zanotto. "DSC method for determining the liquidus temperature of glass-forming systems." Journal of the American Ceramic Society 93.11 (2010): 3757-3763.